ChemComm

COMMUNICATION

View Article Online
View Journal | View Issue

Cite this: *Chem. Commun.*, 2019, 55, 7179

Received 27th April 2019,
Accepted 24th May 2019

DOI: 10.1039/c9cc03271a

rsc.li/chemcomm

A highly conductive, transparent molecular charge-transfer salt with reversible lithiation†

Ying-Shi Guan,[ab] Yong Hu,[ab] Hanguang Zhang,[c] Gang Wu,*[c] Hao Yan*[d] and Shenqiang Ren*[ab]

Here, we describe the high conductivity in a molecular charge-transfer hydrocarbon both as a bulk solid and films. In particular, the high electrical conductivity (~30 S cm^{-1}) and transparency (~80%) of the TTF–TCNQ thin film allowed us to develop its application in all-organic freestanding photodetectors. More importantly, the fabricated TTF–TCNQ thin film can be used as a lithium-ion battery electrode with a specific capacity of ~250 mA h g^{-1}.

Metallic conduction in conjugated polymers has been extensively studied in poly(3,4-ethylenedioxythiophene, (PEDOT)) doped with poly(4-styrenesulfonate, (PSS)), polyaniline, and polypyrrole.[1–3] Although numerous potential applications are emerging, the tremendous influences of molecular packing and intentional doping are still a matter of discussion. Up to now, it is still a challenge to synthesize high-performance metallic polymers due to their complex synthetic procedures with low yields. Secondly, achieving high conductivity is confined to chemical doping which can reversely affect the stability of the polymer materials. Thirdly, the macromolecular backbone structure of conjugated polymers usually provides poor transparency at the visible range.[4] To address these challenges, molecular metals have been reported in certain charge-transfer (CT) salts,[5–7] in which the counter ions can stabilize the charge carriers and strong molecular interaction can be generated simultaneously.

Metallic conduction in molecular aromatic hydrocarbon materials, as a new class of electronic solids, requires strong intermolecular orbital interaction between the molecules and high carrier density.[8,9] It was found that the metallic conductivity of molecular salts is associated with their crystal structures, π-electron overlap, and charge-transfer interactions.[10] Depending on the nature of the interaction between the electrons, a quasi-one-dimensional system may exist in different electronic states.[11] Extensive efforts have been devoted to studying molecular metal tetrathiafulvalene–tetracyanoquinodimethane (TTF–TCNQ), in which the electrons in the highest occupied molecular orbital (HOMO) of the TTF donor molecule are transferred to the lowest unoccupied molecular orbital (LUMO) of the TCNQ acceptor.[12–15] As a result, the TTF and TCNQ chains behave as a quasi-one-dimensional electronic system which shows metallic conductance along the π-overlap stack (*b*-axis), in a wide temperature range from room temperature down to 54 K where the Peierls transition is observed. While the low work function of TTF–TCNQ makes it suitable as a contact material, a strongly anisotropic electrical conductivity along the *a*-axis and *b*-axis of the pseudo-one-dimensional TTF–TCNQ metal makes it challenging for use in electronics.[16–22] Here, we report high conductivity in a molecular TTF–TCNQ solid, in which the pressure-dependent packing structure is studied with regard to the electronic conductivity. A high electrical conductivity (~30 S cm^{-1}) and transparency (~80%) of the TTF–TCNQ thin films, as well as a low contact resistance with the conjugated polymers, enable the development of all-organic freestanding photodetectors with a low bias voltage, suggesting its application potential for transparent molecular electronics. The transparent TTF–TCNQ electrode further enables reversible Li storage, as a new type of anode material for lithium-ion batteries with a specific capacity of ~250 mA h g^{-1}.

The choice of TTF donor and TCNQ acceptor molecules is motivated by the synthesis of organic metallic crystals (Fig. 1a), where a low contact resistance at the organic interface is indispensable to enable organic electronics. The TTF–TCNQ crystal comprises uniformly segregated and parallel stacks of TTF and TCNQ with the π–π molecular orbitals being primarily overlapped along the stacking direction, leading to 1D metallic

[a] *Department of Mechanical and Aerospace Engineering, University at Buffalo, The State University of New York, Buffalo, NY 14260, USA. E-mail: shenren@buffalo.edu*
[b] *Research and Education in eNergy, Environment and Water (RENEW) Institute, University at Buffalo, The State University of New York, Buffalo, NY 14260, USA*
[c] *Department of Chemical and Biological Engineering, University at Buffalo, The State University of New York, Buffalo, NY 14260, USA. E-mail: gangwu@buffalo.edu*
[d] *Center for High Pressure Science and Technology Advanced Research, Shanghai, 201203, P. R. China. E-mail: yanhao@hpstar.ac.cn*

† Electronic supplementary information (ESI) available. See DOI: 10.1039/c9cc03271a

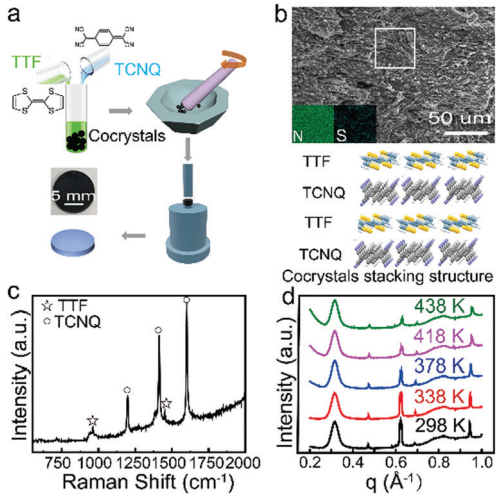

Fig. 1 (a) The schematic diagram for the fabrication of the TTF–TCNQ bulk samples. (b) The SEM image of the TTF–TCNQ pellet and the stacking structure of the TTF–TCNQ cocrystals. (c) The Raman spectrum of the TTF–TCNQ crystals. (d) The XRD data of the TTF–TCNQ crystal under different temperatures.

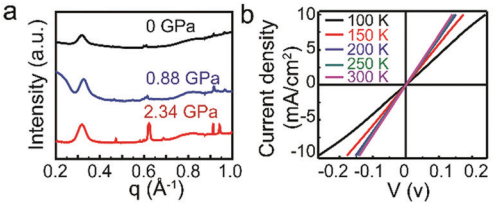

Fig. 2 (a) The XRD data of the TTF–TCNQ crystal under different pressures. (b) The *I*–*V* curves of the TTF–TCNQ bulk samples at different temperatures.

transport behavior. The overlap of the π orbitals along the stack direction causes a giant anisotropic conductivity. This unique molecular stacking structure enables the TTF–TCNQ to exhibit a record room-temperature high conductivity in molecular materials. The as-grown TTF–TCNQ single crystals are then ground and pressed to prepare a solid pellet with a diameter of 10 mm. The structural morphology and chemical composition mapping of the pellet were investigated using scanning electron microscopy (SEM) and energy-dispersive X-ray spectroscopy (EDS, Fig. 1b), which suggests the uniform distribution of the TTF–TCNQ cocrystal. The characteristic principal vibration modes at 1202 cm^{-1} (C═CH bending), 1412 cm^{-1}(C–CN wing stretching), 1603 cm^{-1} (C═C ring stretching), and 2208 cm^{-1} (CN stretching) confirm the presence of the TTF and TCNQ phases in the pellet (Fig. 1c).[23] *In situ* temperature-dependent synchrotron X-ray powder diffraction suggests the stability of the TTF–TCNQ crystal pellet from 298 K to 438 K (Fig. 1d), while the molecular ordering gradually decreases as the temperature is raised further.

In addition, pressure, as one of the thermodynamic variables, can drastically alter the lattice and electronic configuration of the TTF–TCNQ crystals. As shown in Fig. 2a, we apply synchrotron X-ray diffractometry to monitor the crystal structure of TTF–TCNQ under different pressures through uniaxial compression, suggesting the pressure effect on the enhancement of molecular ordering and electronic density.[24] The resistances of the pellets under different pressures are measured in a ^{4}He cryostat with the temperature range from 300 K to 4.2 K (Fig. S1, ESI†). The pressure dependence influences the interaction of the electronic wave functions between TTF and TCNQ, which can increase the overlap of the π–π molecular orbitals to alleviate the quasi-one-dimensional conductivity of TTF–TCNQ.[16,25] The conductivity increases on raising the uniaxial compression, which provides a powerful tool to study the dominant microscopic interaction that drives the anisotropic overlapping integrals between the adjacent molecules. In addition, the pressure induced modulation of the charge transfer ratio between TTF and TCNQ can lead to the commensurability of the charge density wave due to the molecular structure packing.[26,27] In addition, the resistivity of the solid does not show the temperature-dependent or thermal stress induced hysteretic behavior. All samples show a consistent Peierls transition at ~54 K (Fig. S1, ESI†), where the resistivity increases sharply. The measurement of the temperature-dependent resistivity of the TTF–TCNQ pellets is of particular interest, while it is essential to employ the four-terminal configuration (Fig. 2b). The resistivity of the TTF–TCNQ pellets ranges from 5.5 × 10^{-3} Ω cm to 4.5 × 10^{-2} Ω cm on decreasing the temperature from 300 K to 100 K, respectively. The resistivity of the TTF–TCNQ solids is observed to gradually increase with decreasing the temperature, suggesting that the charge transport is dominant by thermally activated hopping.

The lack of flexibility in these molecular crystal powders made it challenging to determine its electronic performance in all-organic electronics. The thin film morphology of the TTF–TCNQ crystals could demonstrate the unique highly conductive feature, optical transparency and low contact resistance with conjugated polymers. Therefore, we evaluate how the charge-transfer nature of the transparent TTF–TCNQ thin films can affect its transport behaviors. The growing thickness of the thin films from 100 nm to 1000 nm, through the evaporation of the TTF–TCNQ single crystals, consists of highly oriented and strongly textured microcrystals composed of high-aspect-ratio nanowires (Fig. 3a, b and Fig. S2, S3, ESI†). The XRD pattern for a typical TTF–TCNQ thin film exhibits (00*l*) reflection, indicating the (002) molecular planes (*ab*-planes) of the films aligned parallel to the substrate surface (Fig. S4, ESI†). The TTF–TCNQ films with different thicknesses have a similar preferential growth orientation revealed by XRD, although the morphology of the thin films with different thicknesses is different due to the different evaporation temperature during the growth process. Fig. 3c presents the transmittance spectra of the TTF–TCNQ thin films, on which the transmittance is decreased from 93% to 36% at 550 nm wavelength with increasing the film thickness from 100 nm to 1000 nm. The thickness dependent electrical conductivity of the TTF–TCNQ films is shown in Fig. 3d. The conductivity is observed to gradually increase with increasing the thickness below 200 nm, while the transmittance is observed to decrease with increasing the thickness. The optimum TTF–TCNQ thin films have a conductivity of 30 S cm^{-1} and transmittance of ~80% at 550 nm wavelength. When compared

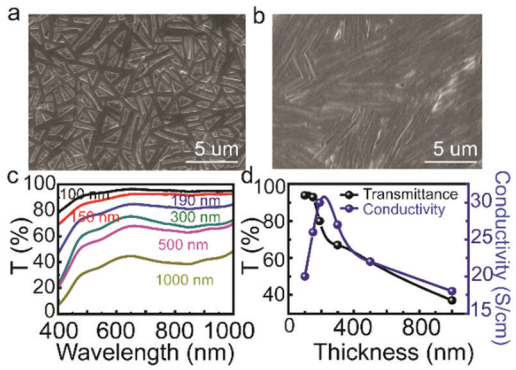

Fig. 3 (a and b) The SEM images of the TTF–TCNQ film with different thicknesses (100 nm for a and 300 nm for b). (c) The transmittance of the TTF–TCNQ film with different thicknesses (from 100 nm to 1000 nm). (d) The thickness dependent transmittance at 550 nm and the thickness dependent conductivities of the TTF–TCNQ film.

with other materials used for transparent electrodes, the performance of TTF–TCNQ is about equivalent to other materials with high transparency and high conductivity.[29]

For the highly conductive TTF–TCNQ thin films with the optimum electric conductivity and transmittance, the temperature-dependent resistivity is studied in the range between 20 K and 298 K based on the four-terminal configuration (Fig. 4a). The resistivity is observed to gradually decrease with an increase in the temperature, suggesting that the charge transport is dominated by thermally activated hopping probability within the TTF–TCNQ films. It should be noted that the Peierls transition (54 K) of the TTF–TCNQ films does not change over the TTF–TCNQ bulk crystals (Fig. S5, ESI†). The resistivity of the TTF–TCNQ film decreases from 2900 Ω cm to 0.033 Ω cm with the temperature increasing from 100 K to 298 K. The conductivity of the bulk TTF–TCNQ is higher than that of the TTF–TCNQ thin films, which is mainly due to the existing grain boundaries in the film samples.

The highly conductive and transparent TTF–TCNQ thin films show great potential for the development of all-organic freestanding electronics.[28] We fabricate flexible photodetectors consisting of the freestanding organic conjugated polymer poly(3-butylthiophene-2,5-diyl)-C_{60} charge transfer complex (Pth-C_{60}) nanosheet and transparent TTF–TCNQ electrode. The current–voltage (*I–V*) characteristics measured in the dark and under illumination with a white light source at different power intensities are shown in Fig. 4b. The maximum responsivity of the photodetector (334 mA W^{-1}) can be calculated using the following equation: $R = I_{ph}/PS$, where I_{ph} is the photocurrent, P is the incident light intensity, and S is the effective area of the device. The on–off photoresponse cycles of the flexible photodetector are shown in Fig. S6 (ESI†), which exhibits a high current on/off ratio of ~21, and high response speed (300 ms). As a comparison, the control photodetector is shown using the freestanding conjugated polymer Pth-C_{60} nanosheet and ITO electrode (Fig. S7, ESI†), the maximum responsivity of which is about 293 mA W^{-1}. The results reveal that the performance of the devices with the TTF–TCNQ thin film electrode is comparable or even better than that of the devices with an ITO electrode.

The profound high conductivity of the molecular TTF–TCNQ film shows its promising lithium storage capability, as a binder-free and carbon conductor-free electrode in a lithium-ion battery. The TTF–TCNQ anode is observed to store lithium ions reversibly at the voltage window between 0.005 V and 3.0 V at a current density of 20 mA g^{-1} for 92 cycles (Fig. 5a). The first cycle of discharge has a capacity of 1026 mA h g^{-1}, while the discharge capacity diminishes to 348 mA h g^{-1} in the second cycle and becomes stable at 220 mA h g^{-1} after 9 cycles (Fig. 5a). The decrease in capacity for the first several cycles is attributed to the formation of a solid electrolyte interphase (SEI), resulting in some irreversible lithiation at low potential. After 90 cycles, the discharge specific capacity still remained 250 mA h g^{-1}, even higher than the capacity at the 9th cycle (220 mA h g^{-1}), which may contribute to the expanded layer structure of TTF–TCNQ to store more lithium ions. When compared with other organic anode materials in lithium-ion batteries, TTF–TCNQ is one of the state-of-art anodes for lithium-ion batteries in terms of small organic molecules (Table S1, ESI†). The voltage-discharge/charge profile reveals the lithium ions interacting with TTF–TCNQ (Fig. 5b). Flat plateaus in the first discharge appear at 2.2 V, suggesting redox reactions with the lithium ions probably taking place on the redox functional groups instead of the phenyl rings.[30] On the other hand, the voltage–discharge profiles

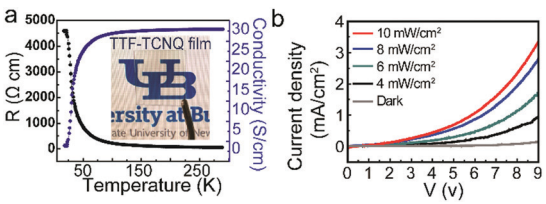

Fig. 4 (a) The temperature-dependent resistivity and conductivity of the TTF–TCNQ film with optimum transparency and conductivity. Inset: the photograph of the TTF–TCNQ film. (b) The current density–voltage curves of the all-organic photodetector under light illumination with different intensities.

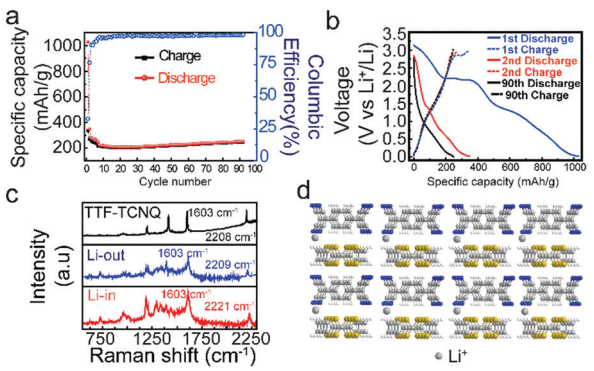

Fig. 5 (a) Cycle performance of the lithium-ion battery using TTF–TCNQ as the anode. (b) The discharging/charging curves of the lithium-ion battery using TTF–TCNQ as the anode. (c) The Raman spectra of the TTF–TCNQ film at different stages of Li intercalation. (d) The schematic diagram of the Li ion storage.

in the 2nd and 90th cycles presented no plateaus, implying the possible lithiation in the layer structure among the phenyl rings.[31] To further confirm the redox reactions position of the TTF–TCNQ-Li interaction, Raman spectroscopy has been used to identify the vibrational modes resulting from different chemical bonds between the Li atoms and TTF–TCNQ complexes. The Raman spectra at different stages of TTF–TCNQ–Li intercalation are shown in Fig. 5c. The characteristic principal vibration mode at 1603 cm^{-1} (C═C ring stretching) and 1202 cm^{-1} (C═CH bending) exhibits no obvious shift, while the vibration mode at 2208 cm^{-1} (C–CN stretching) changes upward to 2221 cm^{-1} at the charge stage and backward to 2209 cm^{-1} at the discharge stage, and in particular, a new vibration mode at 1337 cm^{-1} (C–CN wing stretching) is observed at the charge stage (Li in state) which can be attributed to the charge transfer interactions between the atomic Li and TCNQ. This result indicates that the Li ions mainly intercalate into the TTF–TCNQ layer through interacting with TCNQ, as depicted in Fig. 5d. The realization of the quasi-one-dimensional TTF–TCNQ conductor with highly conductive charge-transfer channels offers unprecedented versatility for lithium-ion transport, which has the potential to assemble lithium-ion batteries.

Given the similarity of highly conductive TTF–TCNQ solids to other charge-transfer complexes, similar consideration of highly conductive transparency and reversible Li storage capability may also hold true for the molecular layered crystals with high charge carrier density. The virtually infinite classes of molecular stacked conductors can provide an unprecedented versatility to tune the electronic properties. The high electrical conductivity of the TTF–TCNQ film with simultaneously high transparency enables the development of all-organic freestanding photodetectors serving as a transparent electrode. Furthermore, our results show that high conductivity and transparency of the TTF–TCNQ thin films have great potential for the development of all-organic transparent freestanding electronics and anode materials in lithium ion batteries.

This work was done at the University at Buffalo (S. R.) and was supported by the U.S. Department of Energy, Office of Basic Energy Sciences, Division of Materials Sciences and Engineering under Award DE-SC0018631 (Physical properties of molecular crystals). The U.S. Army Research Office supports S. R. under Award W911NF-18-2-0202 (Self-assembly of organic crystals). H. Y. would like to acknowledge the support of NSAF (Grant No. U1530402).

Conflicts of interest

There are no conflicts to declare.

Notes and references

1 I. Y. Choi, J. Lee, H. Ahn, J. Lee, H. C. Choi and M. J. Park, *Angew. Chem., Int. Ed.*, 2015, **54**, 10497–10501.
2 B. J. Worfolk, S. C. Andrews, S. Park, J. Reinspach, N. Liu, M. F. Toney, S. C. B. Mannsfeld and Z. Bao, *Proc. Natl. Acad. Sci. U. S. A.*, 2015, **112**, 14138–14143.
3 D. D. Ateh, H. A. Navsaria and P. Vadgama, *J. R. Soc., Interface*, 2006, **3**, 741–752.
4 Y. Joo, V. Agarkar, S. H. Sung, B. M. Savoie and B. W. Boudouris, *Science*, 2018, **359**, 1391–1395.
5 Y. Hu, G. Zhong, Y.-S. Guan, N. H. Lee, Y. Zhang, Y. Li, T. Mitchell, J. N. Armstrong, J. Benedict, S.-W. Hla and S. Ren, *Adv. Mater.*, 2019, **31**, 1807178.
6 Y. Hu, G. Zhong, Y.-S. Guan, J. N. Armstrong, C. Li, C. Liu, A. N'Diaye, A. Bhattacharya and S. Ren, *Small*, 2019, **15**, 1900299.
7 Y.-S. Guan, Y. Hu, Y. Huang, A. F. Cannella, C. Li, J. N. Armstrong and S. Ren, *ACS Appl. Nano Mater.*, 2019, **2**, 1140–1145.
8 D. Jérome, Organic Conductors, *Chem. Rev.*, 2004, **104**, 5565–5592.
9 Y. Kobayashi, T. Terauchi, S. Sumi and Y. Matsushita, *Nat. Mater.*, 2017, **16**, 109–114.
10 H. Alves, A. S. Molinari, H. Xie and A. F. Morpurgo, *Nat. Mater.*, 2008, **7**, 574–580.
11 L. Zuppiroli, S. Bouffard, K. Bechgaard, B. Hilti and C. W. Mayer, *Phys. Rev. B: Condens. Matter Mater. Phys.*, 1980, **22**, 6035–6043.
12 T. Kawamoto, K. Kurata, T. Mori and R. Kumai, *Magnetochemistry*, 2017, **3**, 14.
13 S. Jeon, P. W. Doak, B. G. Sumpter, P. Ganesh and P. Maksymovych, *ACS Nano*, 2016, **10**, 7821–7829.
14 J. Fraxedas, S. Molas, A. Figueras, I. Jiménez, R. Gago, P. Auban-Senzier and M. Goffman, *J. Solid State Chem.*, 2002, **168**, 384–389.
15 K. Shibata, H. Wada, K. Ishikawa, H. Takezoe and T. Mori, *Appl. Phys. Lett.*, 2007, **90**, 193509.
16 C. W. Chu, J. M. E. Harper, T. H. Geballe and R. L. Greene, *Phys. Rev. Lett.*, 1973, **31**, 1491–1494.
17 V. Solovyeva, A. Cmyrev, R. Sachser, H. Reith and M. Huth, *J. Phys. D: Appl. Phys.*, 2011, **44**, 385301.
18 M. J. Cohen, L. B. Coleman, A. F. Garito and A. J. Heeger, *Phys. Rev. B: Solid State*, 1974, **10**, 1298–1307.
19 M. Sakai, M. Iizuka, M. Nakamura and K. Kudo, *Synth. Met.*, 2005, **153**, 293–296.
20 S. Haas, Y. Takahashi, K. Takimiya and T. Hasegawa, *Appl. Phys. Lett.*, 2009, **95**, 022111.
21 M. Sakai, M. Nakamura and K. Kudo, *Appl. Phys. Lett.*, 2007, **90**, 062101.
22 Y. Takahashi, T. Hasegawa, Y. Abe, Y. Tokura and G. Saito, *Appl. Phys. Lett.*, 2006, **88**, 073504.
23 Goudappagouda, S. Chithiravel, K. Krishnamoorthy, S. W. Gosavi and S. Santhosh Babu, *Chem. Commun.*, 2015, **51**, 10439–10442.
24 R. H. Friend, M. Miljak and D. Jérome, *Phys. Rev. Lett.*, 1978, **40**, 1048–1051.
25 C. Weyl, D. Jérome, P. M. Chaikin and K. Bechgaard, *J. Phys.*, 1982, **43**, 1167–1172.
26 Y. Singh, *Adv. Mater. Phys. Chem.*, 2017, **07**, 375–394.
27 K. Murata, K. Yokogawa, S. Arumugam and H. Yoshino, *Crystals*, 2012, **2**, 1460–1482.
28 M. Vosgueritchian, D. J. Lipomi and Z. Bao, *Adv. Funct. Mater.*, 2012, **22**, 421–428.
29 Y. H. Kim, C. Sachse, M. L. Machala, C. May, L. Müller-Meskamp and K. Leo, *Adv. Funct. Mater.*, 2011, **21**, 1076–1081.
30 Y. Hanyu and I. Honma, *Sci. Rep.*, 2012, **2**, 453.
31 H. J. Yen, H. Tsai, M. Zhou, E. F. Holby, S. Choudhury, A. Chen, L. Adamska, S. Tretiak, T. Sanchez and S. Iyer, *Adv. Mater.*, 2016, **28**, 10250–10256.

